Supporting information

High Temperature Interactions of Lead Palmitate with Linseed Oil

Ruslan Barannikov[1,2], Joen Hermans[3,4,5], Jiří Plocek[1], Petr Bezdička[1], Anna Vykydalová[1], Andrii Mahun[6], Libor Kobera[6], Silvie Švarcová[1*]

[1]Institute of Inorganic Chemistry of the Czech Academy of Sciences, Husinec 1001, 250 68 Husinec-Řež, Czech Republic
[2]Department of Inorganic Chemistry, Faculty of Science, Charles University in Prague, Hlavova 2030/8, 128 40 Prague, Czech Republic
[3]Van 't Hoff Institute for Molecular Sciences, University of Amsterdam, PO Box 94157, 1090GD Amsterdam, The Netherlands
[4]Conservation & Restoration, Amsterdam School of Heritage, Memory and Material Culture, University of Amsterdam, PO Box 94552, 1090GN Amsterdam, The Netherlands
[5]Conservation & Science, Rijksmuseum, Hobbemastraat 22, 1071ZC Amsterdam, The Netherlands
[6]Institute of Macromolecular Chemistry of the Czech Academy of Sciences, Heyrovskeho nam. 2, 162 00, Prague 6, Czech Republic

*corresponding author: e-mail: svarcova@iic.cas.cz, phone number: +420 311 236 946;

e-mails: barannikov@iic.cas.cz, j.j.hermans@uva.nl, plocek@iic.cas.cz, bezdicka@iic.cas.cz, vykydalova@iic.cas.cz, mahun@imc.cas.cz, kobera@imc.cas.cz, svarcova@iic.cas.cz

Table of content

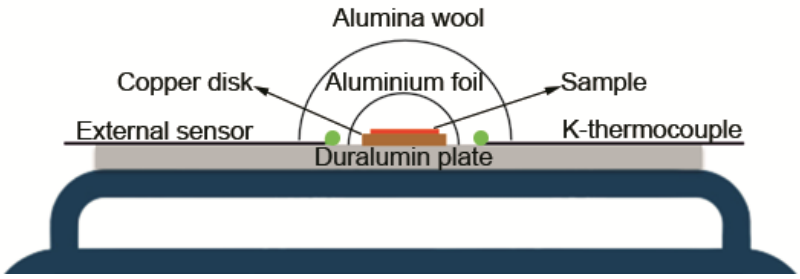

Fig. S1 Experimental setup used to prepare $Pb(C16)_2$+LO_112°C sample

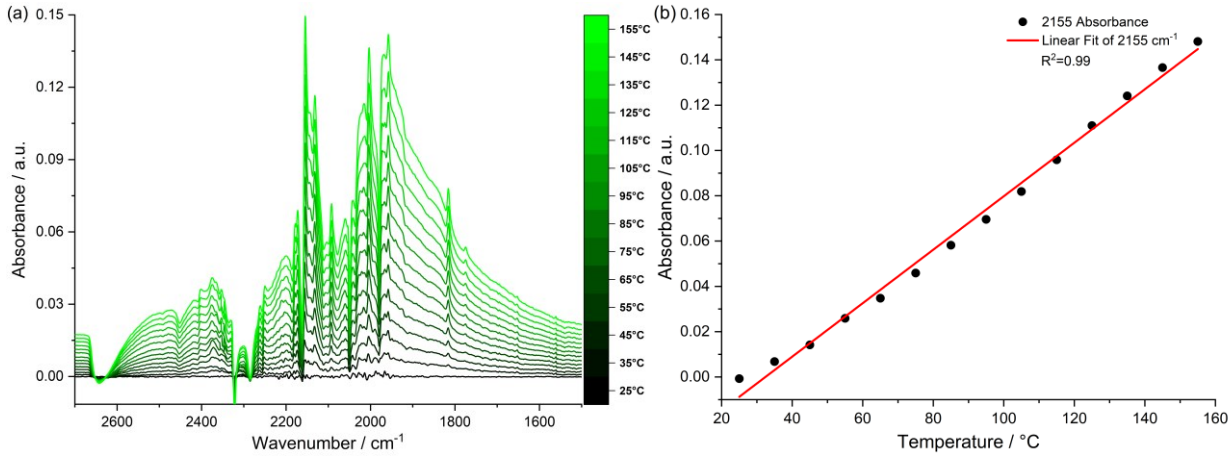

Fig. S2 A sequence of ATR-FTIR spectra acquired in the absence of a sample, ranging from 25 to 155 °C, with a reference baseline set at 25 °C, revealing the temperature-related variations in the ATR diamond's phonon signal (a). A linear regression analysis applied to the intensity at 2155 cm^{-1}, illustrating the background signal exhibits an approximately linear correlation with temperature (b). This finding establishes the diamond's background signal as a reliable "thermometer" enabling the precise monitoring of sample temperature in temperature-dependent ATR-FTIR experiments

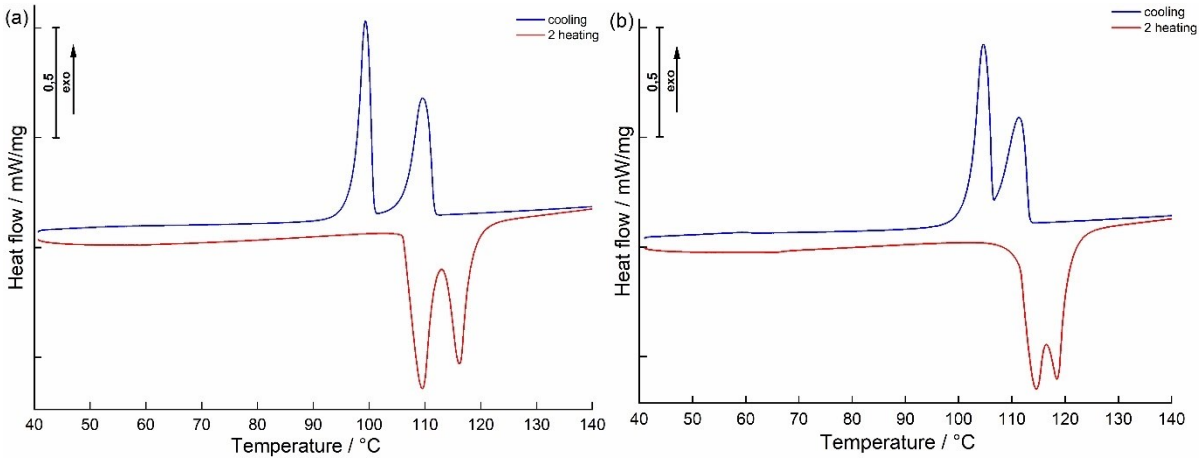

Fig. S3 DSC records of powder $Pb(C16)_2$ (a) and $Pb(C18)_2$ (b)

Table S1 The melting temperatures (T_m), melting enthalpies (ΔH_m) and crystallization temperatures (T_c), crystallization enthalpies (ΔH_m^c) values for powder $Pb(C16)_2$ and $Pb(C18)_2$. Enthalpies are calculated based on total sample weight

Sample	*Phase transition*	*2nd heating*		*cooling*	
		T_m/ ℃	ΔH_m / J/g	T_c/ ℃	ΔH_m^c / J/g
$Pb(C16)_2$	SII↔SI	109.5	149.4	99.6	-147.4
	SI↔IL	116.2		110.1	
$Pb(C18)_2$	SII↔SI	114.3	155.7	104.7	-153.8
	SI↔IL	118.7		111.9	

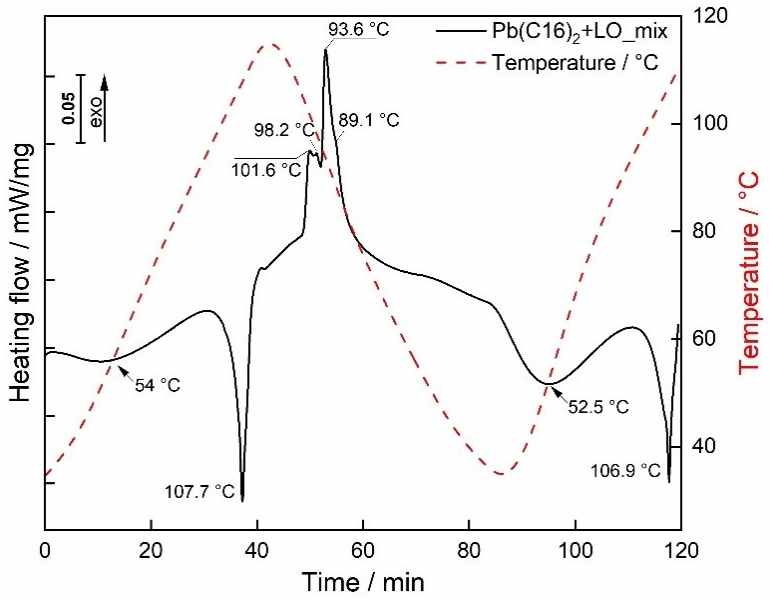

Fig. S4 Reproduced DSC measurement of $Pb(C16)_2$+LO_mix

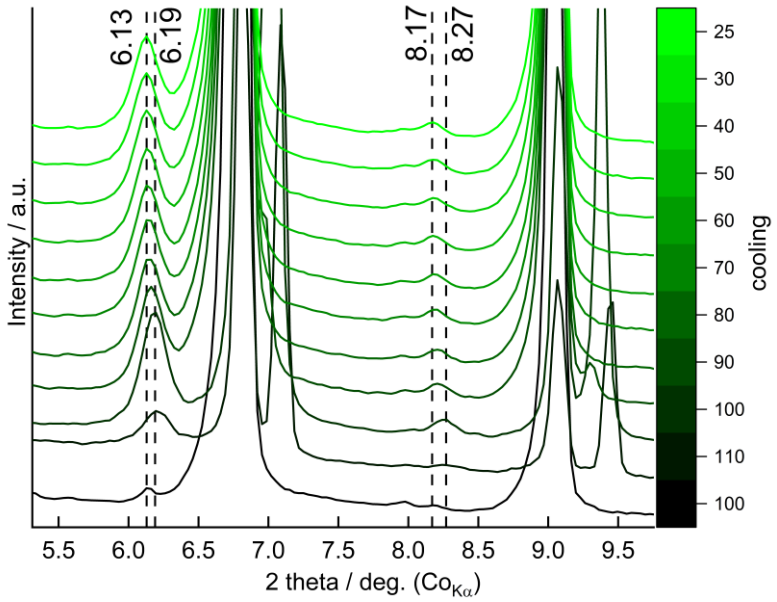

Fig. S5 In-situ high-temperature XRPD patterns of Pb(C16)$_2$+LO_mix during cooling. The dashed lines indicate shifting of additional diffraction signals

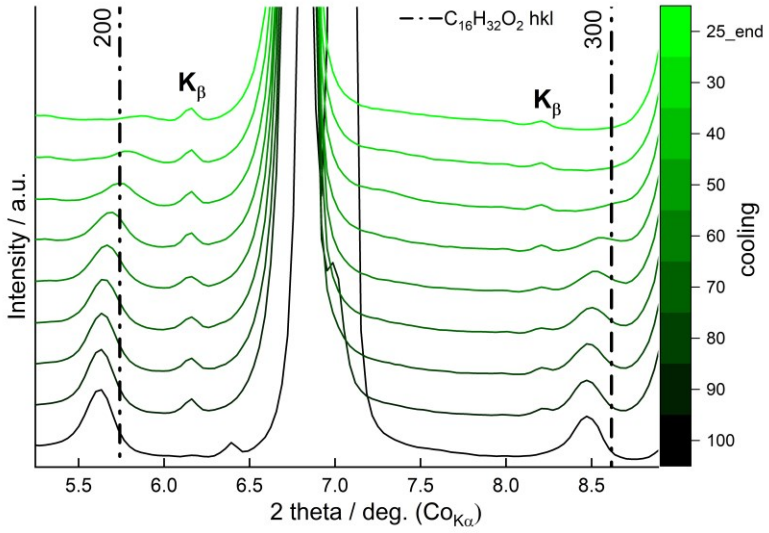

Fig. S6 In-situ high-temperature XRPD patterns of powder Pb(C16)$_2$ during cooling from 100-25 °C. The dashed lines indicate hkl positions of crystalline palmitic acid at room temperature

Free Fatty acid content in linseed oil

A) High-resolution Nuclear Magnetic Resonance (HR-NMR)

^{1}H and ^{13}C HR-NMR spectra were recorded using a Bruker Avance III 600 spectrometer (14.1 T) operating at 600.2 MHz and 150.9 MHz for ^{1}H and ^{13}C respectively. The sample was dissolved in deuterated chloroform ($CDCl_3$-d) and the NMR experiments were performed at 298 K. ^{1}H NMR spectrum was acquired by applying a 90° pulse (width = 18 μs) with a 10 s recycle delay and 32 scans. ^{13}C NMR spectra were recorded using a 14 μs 90° pulse with 13 s recycle delay and 4k scans. Proton decoupling (inverse-gated mode) was used for removing heteronuclear ^{1}H-^{13}C interactions.
The ^{1}H chemical shifts were calibrated using residual proton signals from the deuterated solvent (7.24 ppm from TMS). The ^{13}C chemical shifts were calibrated using signal from the solvent (77.23 ppm from TMS). The spectra were processed using Bruker TopSpin 4.1.1 software.

^{1}H HR-NMR spectrum of the linseed oil sample was recorded and analyzed. The spectrum (Fig. S7) displays a set of signals corresponding to triglycerides (TGs) commonly found in linseed oil.[1] The signal assignment has been done based on literature data.[2-4] Since the signals from the triglycerides and free fatty acids (FFAs) that might be present in the sample are overlapped, the ^{13}C HR-NMR experiment has been performed to resolve the presence of FFAs. In order to do this, the carbonyl region (see magnification in Fig. S8) can be used.[5,6] In this region, the FFAs are easily distinguished from triglycerides since they yield signals in a range of 174-180 ppm whereas the signals from triglycerides are typically found in the 170-174 ppm range.[3,6] Therefore, it is evidenced that the investigated sample contains a small amount of FFAs giving ^{13}C NMR signal at 177.37 ppm. Based on the comparison of the integral intensity of the signals corresponding to FFAs with those corresponding to triglycerides the molar content of the former can be estimated using the following equation:[5]

$$Mol\%\ FFAs = \frac{I_{FFAs}}{I_{FFAs} + I_{TGs}} \qquad \text{(eq 1)}$$

where I_{FFA} is the integral of the free fatty acids carbonyl region, and I_{TGs} is the integral of the triglycerides carbonyl region. Using equation 1 the total content of the FFAs in the investigated sample was evaluated to be 4 (±0.5) mol%.
Furthermore, chromatography was used to separate FFAs and TGs, and ^{13}C HR-NMR experiment was performed on FFAs-rich fraction. This was done in order to determine which free acids were present in the linseed oil sample. Fig. S9 displays a set of signals inherent to unsaturated and saturated fatty acids. Since linseed oil typically consists of triglycerides formed by linolenic, linoleic, oleic, stearic, and palmitic acids,[1] the presence of these acids in a free form in the investigated linseed oil is suggested. All of the above-mentioned acids were detected in the obtained ^{13}C NMR spectrum (Fig. S9) based on analysis of chosen peaks (methyl and vinyl carbons) position and its comparison with the literature data.[7-10] Furthermore, based on the integral intensity of the respective signals, the quantitative content of each acid was obtained and is summarized in Table S2. It was found that the majority of acids (88 mol% in total) in the mixture are unsaturated, with linolenic acid as a main component (58 mol%), and the rest 12 mol% are saturated acid(s). Since stearic and palmitic acids possess similar structures and yield similar NMR signals, it is impossible to distinguish them in the mixture using the ^{13}C NMR spectrum. However,

assuming even decomposition of triglycerides, the presence of both acids is suggested. The obtained ratio of FFAs is consistent with the total content of FAs in TGs of linseed oil reported in the literature[1] and experimentally measured within this research.

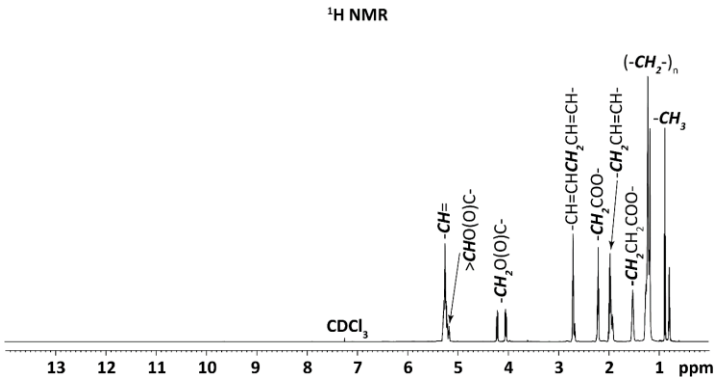

Fig. S7 ^{1}H NMR spectrum of linseed oil sample

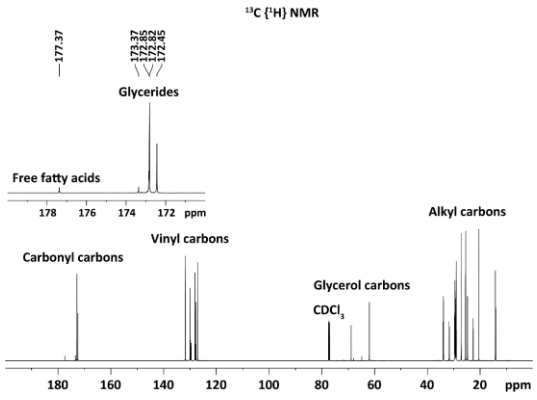

Fig. S8 ^{13}C {^{1}H} NMR spectrum of linseed oil

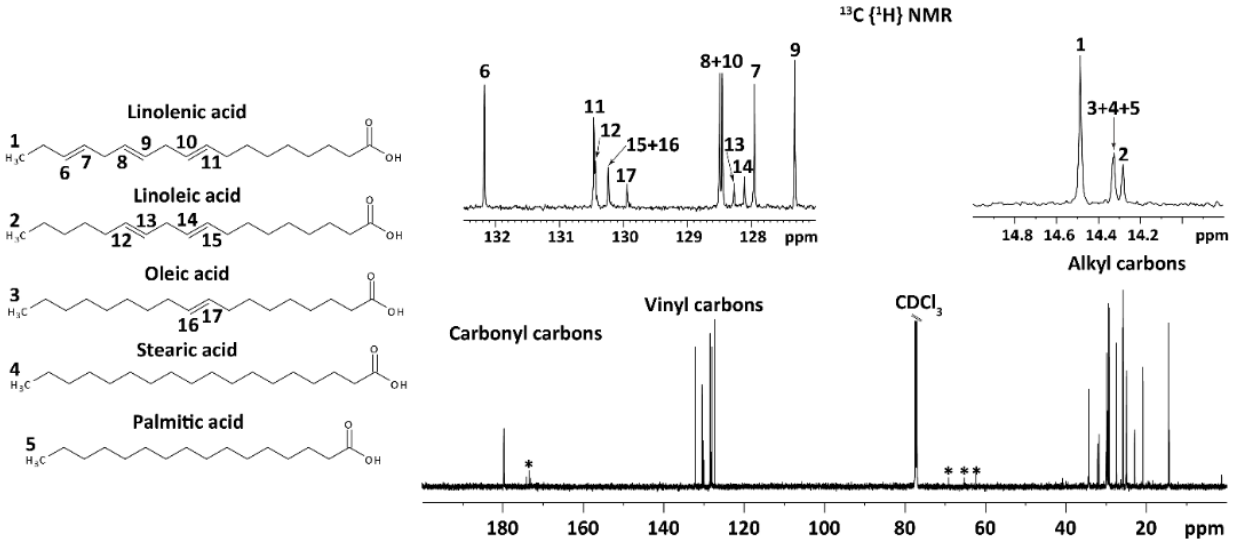

Fig. S9 ^{13}C {^{1}H} NMR spectrum of free fatty acids separated from the linseed oil sample. Signals denoted by an asterisk (*) originate from the triglycerides residuals

Table S2 Content of particular FFAs in a FFAs fraction separated from linseed oil*

Fatty acid	*Content, mol%*
α-Linolenic	58
Linoleic	16
Oleic	14
Stearic/Palmitic	12

*total FFAs content in LO is 4.0 ± 0.5 mol %

B) Determination of fatty acids in linseed oil by GC-FID analysis

The fatty acid profile of the linseed oil used for mixture with lead palmitate was analyzed by gas chromatography with flame ionization detector (GC-FID) according to a certified procedure in the Metrological and Testing Laboratory of University of Chemistry and Technology Prague (Testing laboratory 1316.2 accredited by the CAI according to the EN ISO/IEC 17025:2018). The determined fatty acids are given in Table S3.

Table S3 Fatty acid composition of linseed oil (mol%)

Fatty acid*	(mol%)
palmitic (C16:0)	5.22
stearic (C18:0)	3.06
vaccenic (C18:1n11c)	1.10
oleic (C18:1n9c)	18.26
linoleic (C18:2n6c)	14.12
α-linolenic (C18:3n3)	50.98
γ-linolenic (C18:3n6)	0.18
arachidic (C20:0)	0.15
cis-11-eicosenoic (C20:1n9)	0.20
cis-11,14,17-eicosatrienoic acid	0.10
behenic (C22:0)	0.11
*the acids of the concentration lower than <0.1 mol% i.e. below the limit of quantitation (LOQ) are not listed	

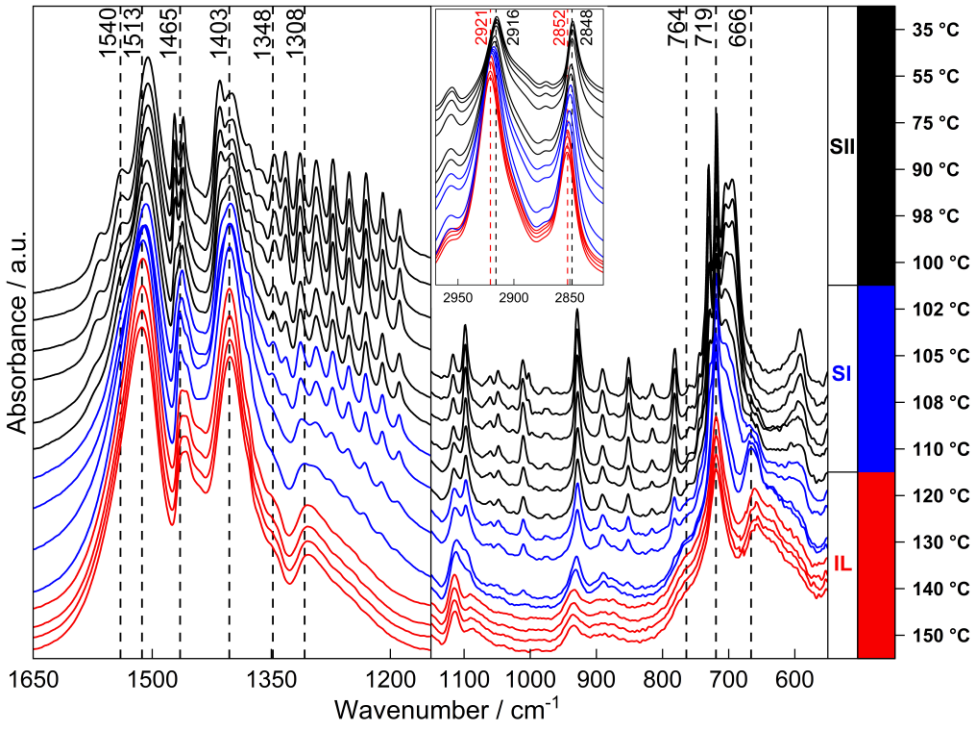

Fig. S10 Temperature dependent FTIR spectra of powder $Pb(C16)_2$ cooling from 150-35 °C

Reproduction of the quenching experiment

X-ray powder diffraction (XRPD) patterns reveal no significant structural differences between the $Pb(C16)_2$+LO_112°C and $Pb(C16)_2$+LO_112°C_rep samples (Fig. S11a). The primary distinction lies in the intensities of the splitting diffraction lines, which reflect varying amounts of the high-temperature phase present in the mixture. FTIR spectrum of $Pb(C16)_2$+LO_112°C_rep, while largely similar to that of $Pb(C16)_2$+LO_112°C, exhibit notable new signals at 1631 cm^{-1} and 1585 cm^{-1} (Fig. S11b).

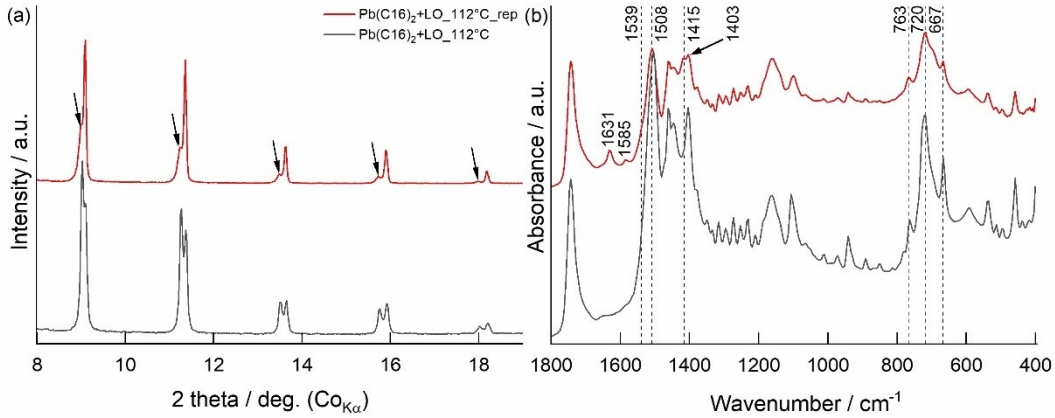

Fig. S11 Comparison of XRPD (a) and FTIR (b) measurement of originally quenched $Pb(C16)_2$+LO_112°C and reproduced samples $Pb(C16)_2$+LO_112°C_rep

These signals have not been previously documented in either the SI phase of lead palmitate or the SII phase of lead octanoate. Several studies have reported the formation of similar bands in the 1630-1500 cm^{-1} region during natural aging or heating of linseed oil in the presence of lead-based pigments.[11-14] Considering the positions of these newly observed bands, it is generally suggested that they are attributed to the formation of lead carboxylates with different coordination structures. However, the formation mechanisms and nature of these newly observed signals remain unknown, making interpretation challenging. Further experiments are necessary to thoroughly investigate this phenomenon. The observed discrepancy between FTIR spectra of the $Pb(C16)_2$+LO_112°C and $Pb(C16)_2$+LO_112°C_rep samples likely result from the inhomogeneity of the quenched sample. Fig. S12 accurately represents this discrepancy when sampling different areas of the specimen.

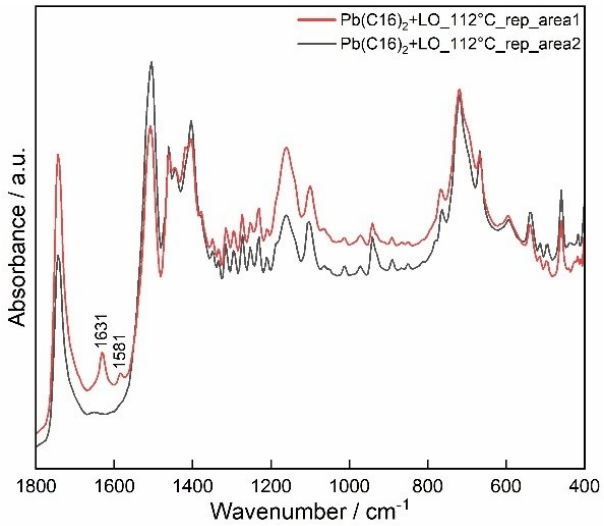

Fig. S12 FTIR spectra of $Pb(C16)_2$+LO_112°C_rep sampled from different areas of the specimen

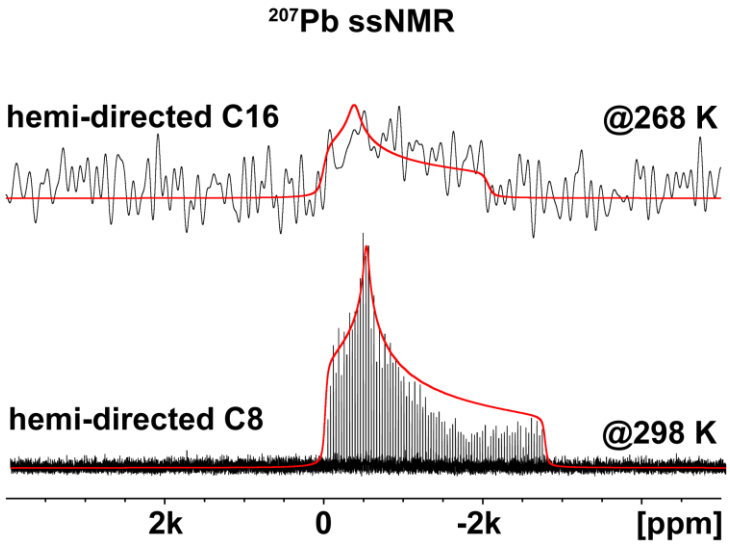

Fig. S13 Experimental ^{207}Pb WURST-CPMG NMR spectrum of hemi-directed $Pb(C8)_2$ compared to high-temperature hemi-directed phase of $Pb(C16)_2$

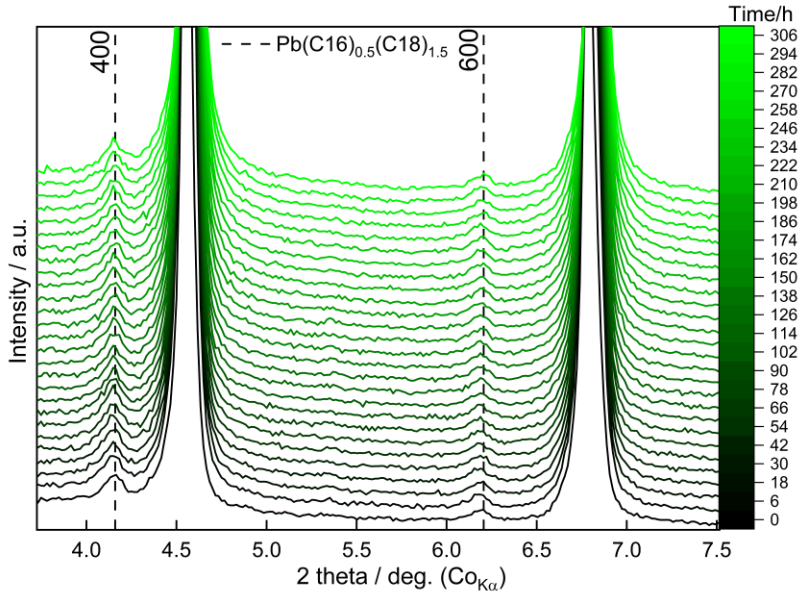

Fig. S14 XRPD pattern of $Pb(C16)_2$+LO_112°C 0h and 306h after quenching

Quantitative phase analysis

The differences between the high and low temperature polymorphs are only visible and clearly distinguishable in the low angle region as the splitting of *h00* diffraction lines. Therefore, we estimated mass fractions of both lead palmitate polymorphs by modifying the Rietveld method to fit the low angle region with the *h00* diffraction lines. However, there is a lack of an appropriate standard for estimating the instrumental broadening in such low angle region. Therefore, we chose the Profex / BGMN software suite which is based on fundamental parameters approach for fitting the diffraction line profiles including the contribution of instrumental broadening[15].

The structural model of the high temperature polymorph of lead palmitate has not been determined yet. The low temperature and high temperature polymorphs are chemically identical and the most important differences lie in the coordination neighborhood of the lead atom. These basal diffraction lines of *h00* family correspond to arrangement of long aliphatic chains of palmitate anions. The splitting of lines is caused by a subtle rearrangement of those chains due to changes in the coordination sphere of Pb atoms. Therefore, we used the constrained models of lead palmitate with the *a* unit cell parameter left to be adjusted for both phases independently. This simplified procedure led to estimation of mass fractions of both polymorphs with the sufficient accuracy that permitted to estimate the kinetic model of the high temperature polymorph transformation.

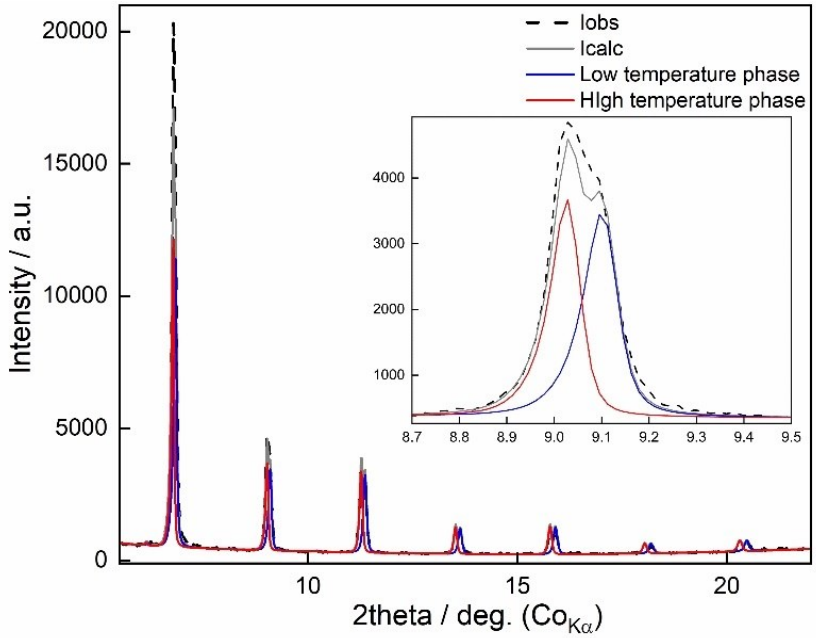

Fig. S15 Structural model of $Pb(C16)_2$ adjusted to fit *h00* lines

The ESD values presented in the table S4 are based on the results of the Rietveld fit. These ESD values represent only the random errors, e.g., counting statistics and/or mathematical procedure of fit. Thus, the values of ESD are obviously smaller than the real bias[16]. In the case of the estimations of mass fractions are the errors calculated as the ESD multiplied by GOF values as recommended by Degen *et al.*[17] for quantitative estimations.

Table S4 Mass fractions w (%) of the high-temperature phase and low-temperature phase obtained during fitting

	High temperature phase			*Low temperature phase*			
Time / h	**w / %**	**ESD**	**ESD*GOF**	**w / %**	**ESD**	**ESD*GOF**	**GOF**
0	53.82	0.99	2.81	46.18	0.99	2.81	2.84
6	48.59	0.96	3.48	51.41	0.96	3.48	3.62
18	47.30	0.91	3.31	52.70	0.91	3.31	3.64
30	45.10	0.86	3.09	54.90	0.86	3.09	3.59
42	44.99	0.86	3.10	55.01	0.86	3.10	3.61
54	44.30	0.85	3.08	55.70	0.85	3.08	3.62
66	42.87	0.85	3.07	57.13	0.85	3.07	3.61
78	42.35	0.85	3.04	57.65	0.85	3.04	3.57
90	41.14	0.81	2.79	58.86	0.81	2.79	3.44
102	39.20	0.79	2.67	60.80	0.79	2.67	3.37
114	38.98	0.78	2.59	61.02	0.78	2.59	3.32
126	37.19	0.76	2.45	62.81	0.76	2.45	3.23
138	36.52	0.78	2.48	63.48	0.78	2.48	3.18
150	34.76	0.77	2.36	65.24	0.77	2.36	3.06
162	32.26	0.73	2.12	67.74	0.73	2.12	2.91
174	29.28	0.72	2.03	70.72	0.72	2.03	2.82
186	28.59	0.72	1.91	71.41	0.72	1.91	2.65
198	26.75	0.74	1.85	73.25	0.74	1.85	2.50
210	25.62	0.82	2.00	74.38	0.82	2.00	2.44
222	23.20	1.00	2.27	76.80	1.00	2.27	2.27
234	22.80	1.10	2.46	77.20	1.10	2.46	2.24
246	19.80	1.20	2.60	80.20	1.20	2.60	2.17
258	19.80	1.50	3.10	80.20	1.50	3.10	2.06
270	16.00	1.50	3.03	84.00	1.50	3.03	2.02
282	14.40	1.50	2.96	85.60	1.50	2.96	1.97
294	12.60	1.40	2.79	87.40	1.40	2.79	1.99
306	12.10	1.50	2.92	87.90	1.50	2.92	1.95
407	12.90	0.85	1.29	87.10	0.85	1.29	1.52
475	12.14	0.83	1.22	87.86	0.83	1.22	1.47
1892	5.65	0.88	1.51	94.35	0.88	1.51	1.71
			Dataset from earlier experiment				
17	50.41	0.52	2.14	49.59	0.52	2.14	4.12
70	38.26	0.24	0.84	61.74	0.24	0.84	3.49
138	18.15	0.52	1.05	81.85	0.52	1.05	2.02
209	7.42	0.62	1.05	92.58	0.62	1.05	1.70
498	0.00			100.00			1.91

* the asterisk-marked values are omitted from plots and data analysis, as they solely indicate transformation completion and were obtained using inconsistent measurement intervals

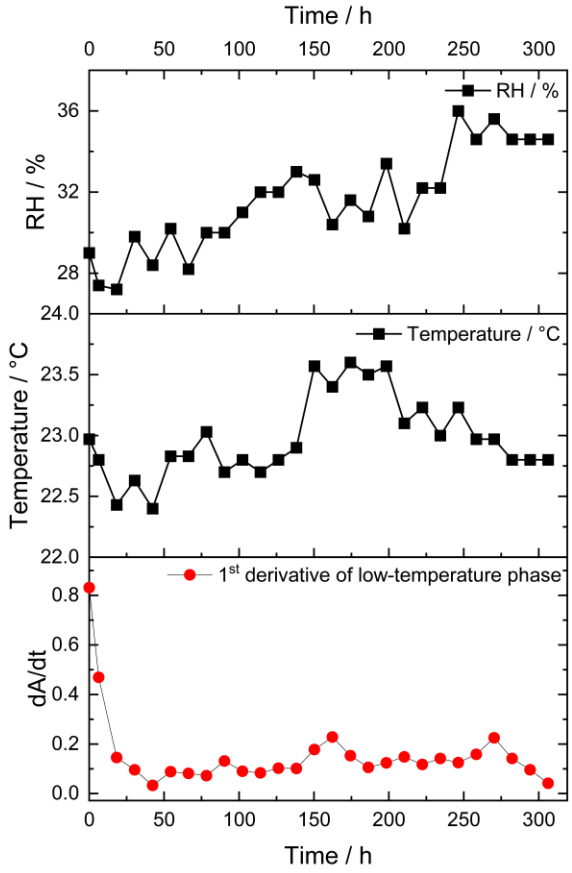

Fig. S16 Comparison of the 1st derivative of low-temperature phase with an average RH and temperature inside diffractometer

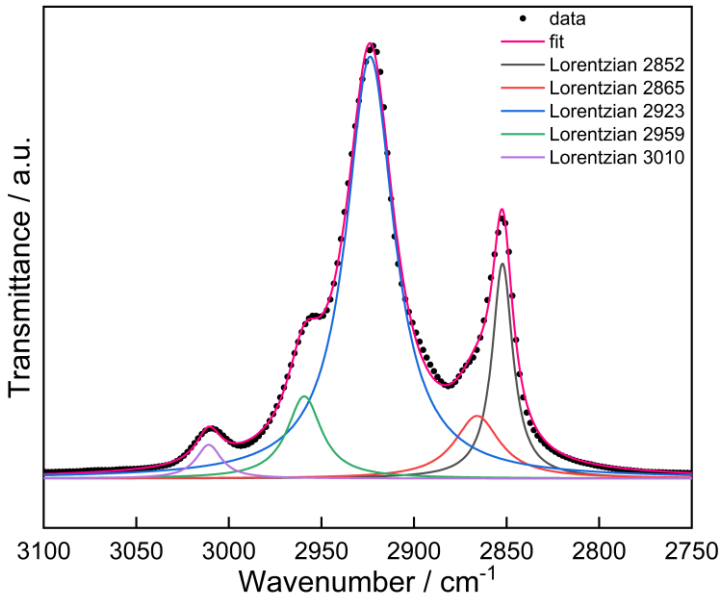

Fig. S17 The FTIR spectrum of $Pb(C16)_2$+LO_112°C was deconvoluted in the region of 3100-2750 cm^{-1} using five Lorentzian band shapes. The deconvolution was performed using non-linear curve fitting in OriginPro 2021, with constraints applied to peak's number and position

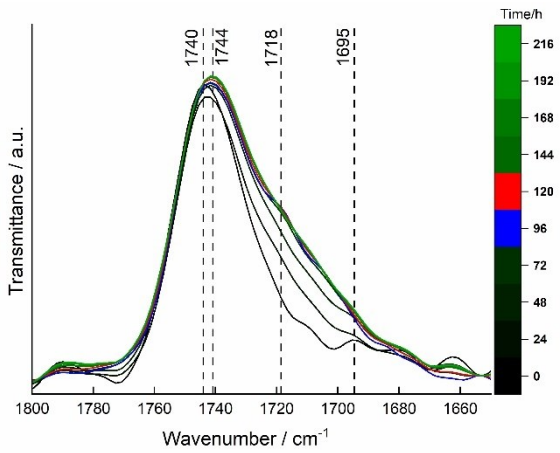

Fig. S18 FTIR spectra of the sample $Pb(C16)_2$+LO_112°C in carbonyl spectra region baseline-corrected at 1850 cm^{-1}

Descriptive kinetics of polymorphic transformation in $Pb(C16)_2$+LO_112°C

This kinetic analysis presents a descriptive model characterizing the phase transformation behavior of lead palmitate dispersed in a linseed oil matrix after quenching. While the analysis does not investigate the underlying molecular mechanisms, it employs a linear fitting approach based on zero-order kinetic equations to quantify the observed transformation.

The linear fits presented in Fig. S19a demonstrate high correlation coefficients ($R^2 > 0.98$) with equal but opposite slopes, indicating a direct transformation between two phases that follows zero-order kinetics. This linear relationship suggests that the transformation rate remains constant and independent of reactant concentration. Comparable fitting parameters were obtained from complementary datasets from earlier experiments, despite having fewer data points and varying measurement intervals (Fig. S19b).

Minor deviations from linearity, along with transformation rate variations observed in the first derivative analysis of the low-temperature phase (Fig. 10) and slight fitting inconsistencies (Fig. S19), likely stem from external factors such as temperature fluctuations, humidity variations, and oil polymerization rather than changes in material concentration.

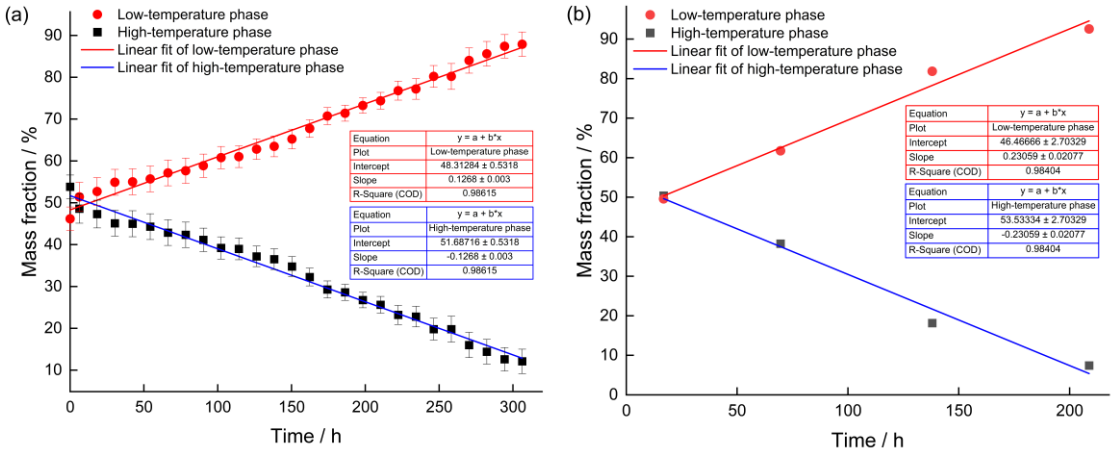

Fig. S19 Fitting of the zero-order kinetic equation applied to (a) the primary dataset and (b) complementary data obtained from a previous experiment

References

1. V. Popa, A. Gruia, D.- Raba, D. Dumbrava, C. Moldovan, D. Bordean and C. Mateescu, *J. Agroaliment. Process. Technol.* 2012, **18,** 136–140.
2. B. Nieva-Echevarría, E. Goicoechea, M.J. Manzanos and M.D. Guillén, *Food Res. Int.*, 2017, **91,**171–182.
3. M. Tŭsar, L. Tŭsar, S. Bohanec and J. Zupan, *J. Chem. Inf. Comput. Sci.*, 1992, **32,** 299–303.
4. M.A. Brescia and A. Sacco, *Mod. Magn. Reson.,* 2008, **chapter**, 1645–1650.
5. M.E. Di Pietro, A. Mannu and A. Mele, *Processes.,* 2020, **8**, 1–15.
6. R. Sacchi, I. Medina, S.P. Aubourg, I. Giudicianni, L. Paolillo and F. Addeo, *J. Agric. Food Chem.,* 1993, **41,** 1247–1253.
7. X. Zhong, R. Song, D. Shan, X. Ren, Y. Zheng, F. Lv, Q. Deng, Y. He, X. Li, R. Li, L. Yan and G. She, *Bioorg. Chem.*, 2023, **140**, 106790.
8. A. Leggio, R. De Marco, F. Perri, M. Spinella and A. Liguori, *European J. Org. Chem.*, 2012, 114–118.
9. W. Xiong, Y. Wang, X. Yang and W.H. Liu, *Org. Lett.,* 2023, **25,** 2948–2952.
10. W.Y. Tan, Y. Lu, J.F. Zhao, W. Chen and H. Zhang, *Org. Lett.*, 2021, **23,** 6648–6653.
11. J. van der Weerd, A. van Loon and J. J. Boon, *Stud. Conserv.,* 2005, **50**, 3–22.
12. R. J. Meilunas, J. G. Bentsen and A. Steinberg, *Stud. Conserv.,* 1990, **35**, 33–51.
13. L. de Viguerie, P. A. Payard, E. Portero, Ph. Walter and M. Cotte, *Prog. Org. Coat.,* 2016, **93**, 46–60.
14. G. DePolo, P. Iedema, K. Shull and J. Hermans, *Macromolecules,* 2024, **57**, 8263–8276.
15. J. Bergmann, P. Friedel and R. Kleeberg, CPD Newsletter (Commission of Powder Diffraction, International Union of Crystallography), 1998, 20, 5–8.
16. I. C. Madsen, N. V. Y. Scarlett, R. Kleeberg, K. Knorr, "Quantitative Phase Analysis", in C. J. Gilmore, J. A. Kaduk, H. Schenk, H., eds. International Tables for Crystallography, Vol. H, Chapter 3.9, pp 344-373, IUCr, 2019, ISBN 978-1-118-41628-0.
17. T. Degen, T. Dortmann, HighScorePlus, version 5.3.0.33005, October 1, 2024, XHP_CHMPrint.pdf file, page 421.